# Virtual Field Campaigns on Deep Tropical Convection in Climate Models

BRIAN MAPES

*Rosenstiel School of Marine and Atmospheric Sciences, University of Miami, Miami, Florida*

JULIO BACMEISTER

*NASA Goddard Space Flight Center, Greenbelt, Maryland*

MARAT KHAIROUTDINOV

*Colorado State University, Fort Collins, Colorado*

CECILE HANNAY

*National Center for Atmospheric Research, Boulder, Colorado*

MING ZHAO

*NOAA/Geophysical Fluid Dynamics Laboratory, Princeton, New Jersey*

(Manuscript received 20 August 2007, in final form 1 July 2008)

ABSTRACT

High-resolution time–height data over warm tropical oceans are examined, from three global atmosphere models [GFDL's Atmosphere Model 2 (AM2), NCAR's Community Atmosphere Model, version 3 (CAM3), and a NASA Global Modeling and Assimilation Office (GMAO) model], field campaign observations, and observation-driven cloud model outputs. The character of rain events is shown in data samples and summarized in lagged regressions versus surface rain rate. The CAM3 humidity and cloud exhibit little vertical coherence among three distinct layers, and its rain events have a short characteristic time, reflecting the convection scheme's penetrative nature and its closure's concentrated sensitivity to a thin boundary layer source level. In contrast, AM2 rain variations have much longer time scales as convection scheme plumes whose entrainment gives them tops below 500 hPa interact with humidity variations in that layer. Plumes detraining at model levels above 500 hPa are restricted by cloud work function thresholds, and upper-tropospheric humidity and cloud layers fed by these are detached from the lower levels and are somewhat sporadic. With these discrete entrainment rates and instability thresholds, AM2 also produces some synthetic-looking noise (sharp features in height and time) on top of its slow rain variations. A distinctive feature of the NASA model is a separate anvil scheme, distinct from the main large-scale cloud scheme, fed by relaxed Arakawa–Schubert (RAS) plume ensemble convection (a different implementation than in AM2). Its variability is rich and vertically coherent, and involves a very strong vertical dipole component to its tropospheric heating variations, of both signs (limited-depth convective heating and top-heavy heating in strong deep events with significant nonconvective rain). Grid-scale saturation events occur in all three models, often without nonconvective surface rain, causing relatively rare episodes of large negative top-of-atmosphere cloud forcing. Overall, cloud forcing regressions show a mild net positive forcing by rain-correlated clouds in CAM3 and mild net cooling in the other models, as the residual of large canceling shortwave and longwave contributions.

*Corresponding author address:* Dr. Brian Mapes, RSMAS/MPO, 4600 Rickenbacker Cswy., Miami, FL 33149-1098.
E-mail: mapes@miami.edu

DOI: 10.1175/2008JCLI2203.1

## 1. Introduction

In this paper, tropical convection in climate models is studied as in nature: via Eulerian ''field campaigns'' of about a month duration, with all processes fully interactive with free-running weather. Because the weather sequences are uncontrolled, our analysis can only be impressionistic and statistical. Monthly mean statistics are used to characterize the sample and focus on a particular regime: rainy marine conditions. This approach may usefully complement traditional climate performance evaluations (e.g., via monthly means), and efforts to drive the model through observed weather sequences in 1D (Randall et al. 1996) or 3D (Boyle et al. 2008), which have their own limitations.

Broadly, we seek better understanding of how climate model performance is related to atmospheric physical processes, parameterized in the vertical domain, at a time-step level. In particular, convection and cloud schemes are thought to be crucial in model shortcomings from tropical biases (Bretherton 2007) to variability simulations (Lin et al. 2006). Since these schemes interact in complex ways with each other and with additional schemes (e.g., the boundary layer), all interacting with resolved dynamics, offline evaluations are of limited utility in predicting true performance. Weather is inescapable in nature, filling the gap between processes and climate, so it seems clear that studies of the weather in climate models are necessary if observations are to play a role in advancing climate modeling capabilities.

The models used here[1] are described in more detail in Wyant et al. (2006), whose Table 1 summarizes the physics schemes. These papers are companions: both arose from the same multi-investigator Climate Process Team (CPT) project on low-latitude cloud feedbacks in climate and both analyze the same model versions. Model output locations (Fig. 1) were chosen to coincide (spatially at least) with available observations in many cases.

Similar analyses of GCM column outputs, including the interesting special case of a GCM with nested cloud models, have also recently been offered by DeMott et al. (2007). Another recent CPT project involving the lead author uses the column output strategy to evaluate models in the North American monsoon region (manuscript in preparation). The Coordinated Energy and Water Cycle Observation Project (CEOP) calls such column outputs Model Output Location Time Series (MOLTS) (Bosilovich and Lawford 2002). Prospects and recommendations for such Eulerian column studies are discussed in the conclusions section.

After a discussion of the data and methods, this paper describes our sorting of columns into regimes based on monthly statistics (section 3), shows sample months in time–height format (section 4), and offers statistical views in lag–height space (section 5) before concluding.

## 2. Data and methods

Observational data from the rawinsonde array budgets of the Kwajalien Experiment (KWAJEX) of 1999 (Sobel et al. 2004) were obtained with 6-hourly and 25-hPa resolution. Blossey et al. (2007) discuss these time–height data, which have been adjusted for energetic consistency, and their use in forcing a doubly periodic 3D cloud model whose hourly outputs are also examined here. Horizontal advective tendencies were prescribed, along with domain-mean vertical velocity, which advected the model's local vertical gradients of static energy and water substances. Horizontal winds were nudged toward the observed on a 2-h time scale. The periodic domain was 256 km $\times$ 256 km with 2-km grid spacing. Sounding array observations from the Large-Scale Biosphere Atmosphere (LBA) experiment in Brazil (Silva Dias et al. 2002) and the Intensive Flux Array (IFA) of Tropical Ocean and Global Atmosphere Coupled Ocean–Atmosphere Response Experiment (TOGA COARE) (Johnson and Ciesielski 2000) were also used (included in Fig. 2 as the characters L and I). More observations were not deemed necessary since results here are largely consistent with data from other field programs analyzed in Mapes et al. (2006) and DeMott et al. (2007).

Global model data were obtained from continuous model runs forced by year 2000 sea surface temperature patterns. The three models examined include the NCAR CAM 3.0, the GFDL AM2p12b, and the NASA NSIPP2 model, a developmental version of an AGCM that shares many of the properties of the NASA Global Modeling and Assimilation Office (GMAO) Goddard Earth Observing System 5 (GEOS5) model released in April 2005. Further details of the models are summarized in companion work (Wyant et al. 2006; physics schemes are summarized in their Table 1).

Data are at 20- (CAM3) or 30-min (AM2 and NSIPP2) resolution, essentially the model ''time step'' resolution, although this oversimplifies the nature of time integration schemes. For example, CAM3 radiation quantities are only updated hourly even though other tendencies are computed more frequently. CAM3 and AM2 data are from the sites shown in Fig. 1 for all months of 2000. NASA

[1] Specifically, the models are the National Center for Atmospheric Research (NCAR) Community Atmosphere Model (CAM3), the Geophysical Fluid Dynamics Laboratory (GFDL) Atmosphere Model 2 (AM2), and the National Aeronautics and Space Agency (NASA) Seasonal-to-Interannual Prediction Project 2 (NSIPP2) model, whose lineage has been renamed, so we call this ''the NASA model.''

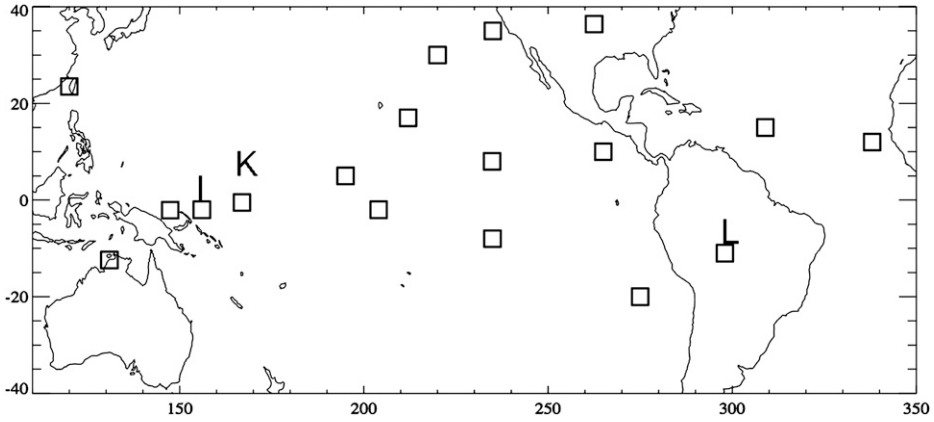


FIG. 1. Base map of the CAM and AM2 output column locations (squares) and observation sites used in Fig. 2: Kwajalein (K), IFA (I), and LBA (L). NASA output locations are not shown (20° spaced longitudes along latitudes 8°N or 8°S.)

data are only for 35-day samples around July, at a set of tropical deep convective sites over ocean (8°N and 8°S at ITCZ sites spaced 20° longitude apart). Data were handled in each model's vertical grid, with vertical axes labeled as pressure based on a reference profile.

The main statistical technique used here is time-lagged linear regression of various fields at various altitudes against a base time series of surface rain rate, following Mapes et al. (2006). Lag-pressure sections of rain-rate regression coefficients for a given calendar month express a characteristic multivariate time structure associated with rain events within that month. The units of these sections are units of predictand/units of predictor—millimeters per hour in this case.

These monthly lag–height sections were further composited across months by simple averaging. The magnitude of the regression coefficient is not strongly sensitive to the number of rain events, that is, to monthly total rainfall, so these multimonth composites take their structure quite evenly from all months entering them. The biggest danger is noisy structure from dry months, but prescreening by monthly rain minimizes this problem. For significance testing, shading in Figs. 6–8 indicates where the mean exceeds the standard deviation at each lag and pressure divided by the square root of the number of months. That is, each month is treated as one degree of freedom. Error ranges on the radiative curves are indicated by plotting a suite of 10 different randomized composites based on different resamplings of about half of the months entering the figure.

## 3. Sorting of site months into climate regimes

The available site months of data are characterized in Fig. 2, via four scatterplots of monthly mean pressure vertical velocity $\omega_{500}$, top-of-atmosphere (TOA) net cloud radiative forcing (CRF), rain rate $R$, and the $R$ submonthly standard deviations (further subdivided into total and diurnal cycle variances). Plotted characters indicate the model (C for CAM3, A for AM2, N for NSIPP2).

Figure 2a, modeled after Fig. 3 of Wyant et al. (2006), shows that clouds in both ascending (negative $\omega_{500}$) and descending (positive) regions predominantly cause negative CRF (cooling of the earth). The model all-tropics mean curves of Wyant et al. are included for reference, and the balanced scatter around these curves indicates that these column months form a reasonable sample of the CAM3 and AM2 regime space. The available NASA columns do not include descending site months. It is notable that the lower-left corner (below $-50, -50$) contains many points here, but is unpopulated in the observational scatter in Fig. 3 of Wyant et al. (although that was based on climatological, not actual, monthly means).

In ascending regions, rain rate $R$ and $\omega_{500}$ are highly correlated, as seen in Fig. 2b. Observational site months lie within the model scatter (''I'' shows four IFA months and the 4-month mean, ''K'' shows KWAJEX and the forced cloud model, and ''L'' indicates the LBA data). Monthly descent tends to correspond to little rain. Since rain within a month tends to occur sporadically, $R$ and its standard deviation are also highly correlated (Fig. 2c). The models seem to lie slightly below observations in terms of their $R$ standard deviation, although this arguably may be appropriate to their spatial resolution.

It is useful to distinguish between land and maritime tropical convection, but many of the columns (following past field experiments) lie in coastal zones. As a practical discriminator of land influence, Fig. 2d shows the

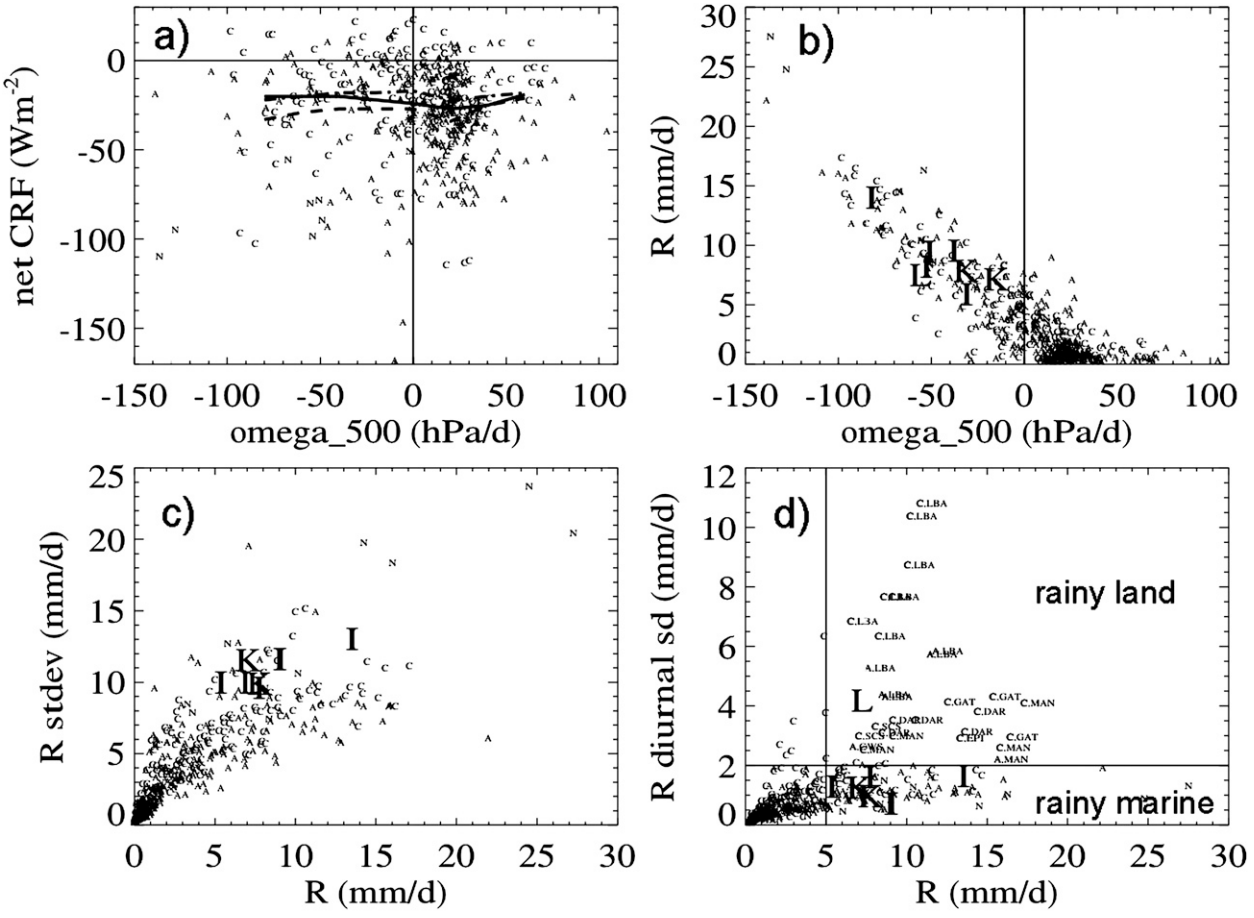


FIG. 2. Scatterplots of monthly mean data from sites shown in Fig. 1. Letter symbols indicate model name as C: CAM3, A: AM2, and N: NSIPP2. In (a) whole tropics model mean curves are transcribed from Fig. 3 of Wyant et al. (2006) as solid: CAM3, dashed: AM2, and dashed–dotted: NASA. In (d) site name indicators are appended to the model name for the rainy land points.

standard deviation of the composite diurnal cycle of $R$ within each month. In the upper-right region (''rainy land'') are many site months over land: LBA; Atmospheric Radiation Measurement Program (ARM; in Oklahoma) site; Darwin, Australia (DAR); and Manus, Papua New Guinea (MAN); but there are also the offshore locations of the GARP Atlantic Tropical Experiment (GATE) and the East Pacific Investigation of Climate (EPIC) experiments in the far eastern tropical Atlantic and Pacific, respectively. Rainy marine months (lower right) are from many sites and cannot be distinguished here.

## 4. Data samples

Before regressing and blending data within regimes, it is useful to examine the texture and detail that can only be appreciated in raw data samples. To facilitate intercomparison, identical plotting conventions are used in Figs. 3–4 , although some fields are not available in some figures. Figures 3a,b show the rawinsonde budget data from KWAJEX. Gray shading denotes relative humidity; the green curve is budget-derived surface rain rate, and colors show apparent heating (Q1) (Yanai et al. 1973). Rain tends to be associated with enhanced deep-layer humidity and with diagnosed heating (red). These deep anomalies tend to slope up and to the right (ascend with time). The time resolution is coarse (6 h), and cloud fraction and condensate fields are omitted for lack of observations.

One estimate of KWAJEX cloud fields was obtained from a cloud model forced with observationally derived advective forcings (Blossey et al. 2007). Hourly cloud model outputs are shown in Figs. 3c,d. Rain events occur at about the right times, driven mainly by observations of horizontal wind divergence (integrated to yield estimates of vertical velocity). Again, these events are associated with deep positive RH and Q1 anomalies, which tend to ascend with time. Cloud condensate accompanies rain events (cloud water + ice + snow; light

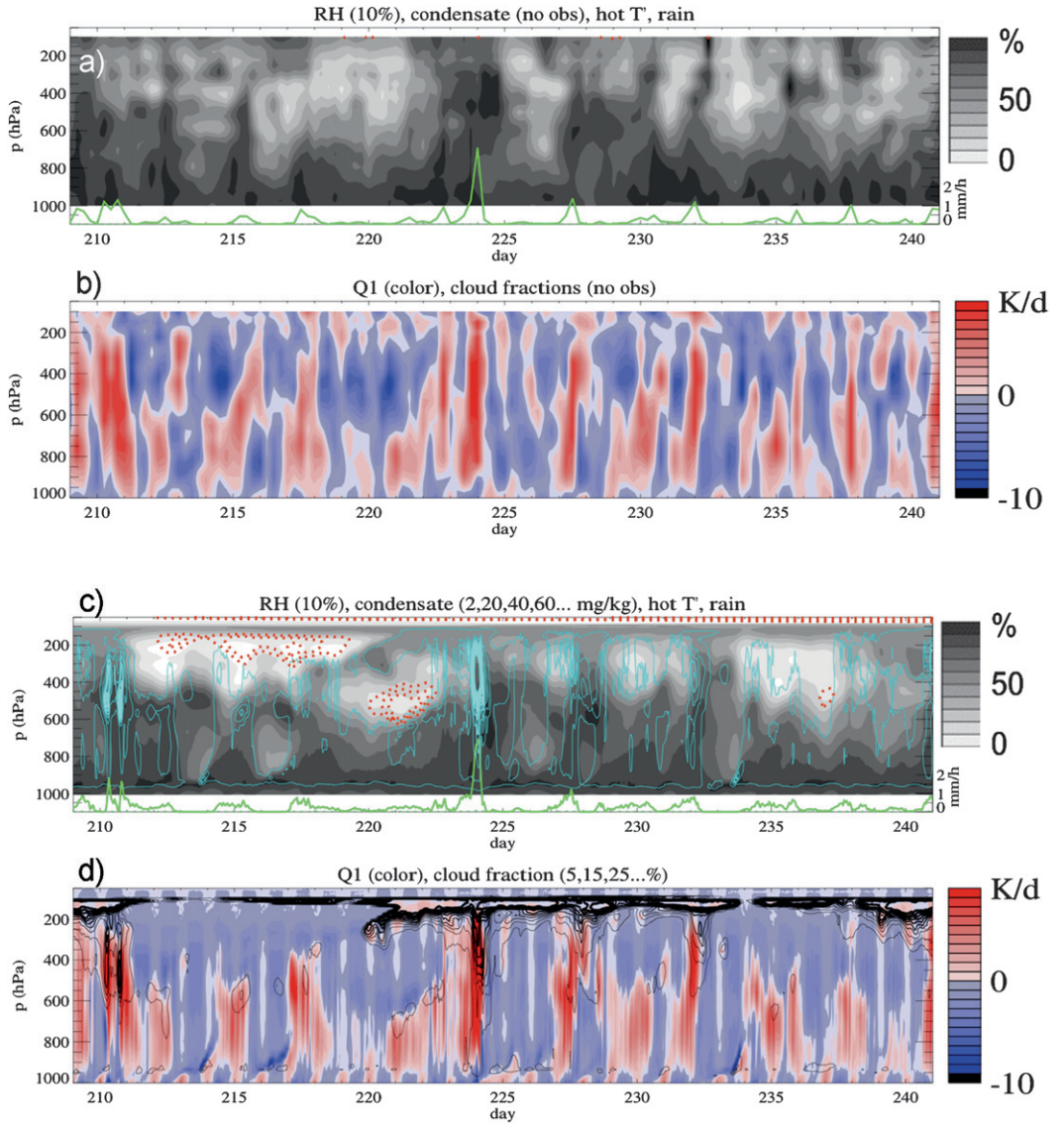


FIG. 3. (a), (b) KWAJEX observations and (c), (d) observation-driven model outputs from a 3D periodic cloud model forced by large-scale advection terms. Gray panels show relative humidity RH, cloud condensate [cyan, not available in (a), contour values are 2, 20, 40, 60, . . . , 200 mg $kg^{-1}$], rainfall time series (green, axis at right), and $T$ deviations from the initial state (red dotted contours 3, 4, and 5 K). Colored panels show budget-derived apparent heat source Q1 and cloud fraction if available [(black contours, not available in (b)]; 32 days in July–August 1999 are shown.

blue contours on RH, note the lowest contour is only 2 mg $kg^{-1}$ to show very low amounts, while the maximum contour of 200 mg $kg^{-1}$ makes large values appear as voids). Large values occur mainly in the middle and upper troposphere, except for low-level cloud water buildups right before forced rain events after dry periods, for example, at the initial time (day 206) and around days 214 and 233.

Cloud fraction (black contours on Q1 plot) is often below 5% (smallest contour). Values of 100% (voids within black contours) are most prominent near 100–150 hPa, where the imperfections of forcing data and model may be especially problematic. Major rain events also have substantial cloud coverage in the middle to upper troposphere (200–600 hPa). A distinct population of low clouds (900–950 hPa) is also seen, with a slight preference for daytime when boundary layer Q1 is positive owing to solar absorption (reds).

The red dotted contours on the RH plot in Fig. 3b illustrate a shortcoming of such forced column (or

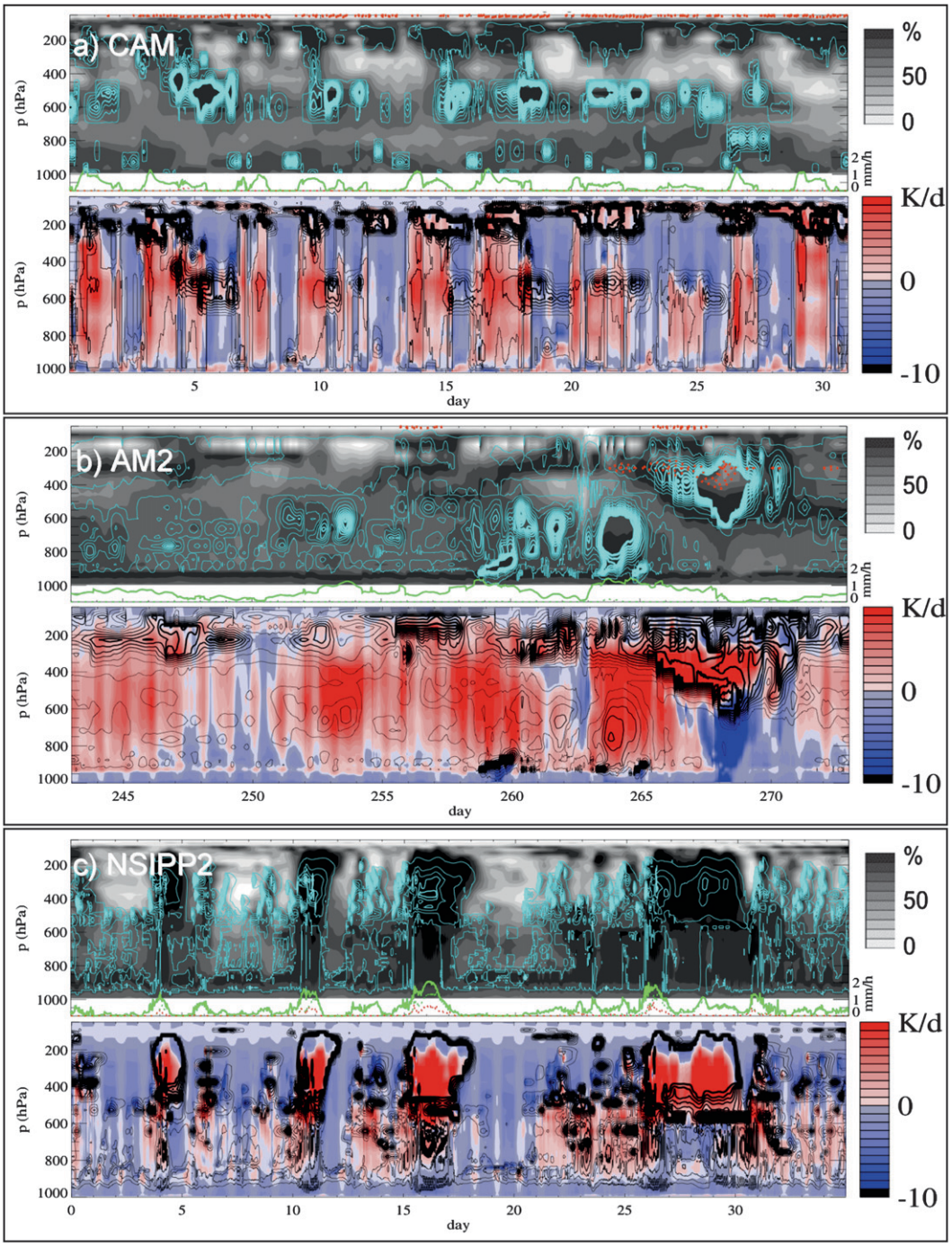


FIG. 4. One-month samples of GCM outputs over the tropical ocean: All quantities and contours as in Fig. 3; large-scale rain rate is also indicated as dotted curves beneath total rain. (a) CAM model at location I on Fig. 1 in January. (b) AM2 model at Manus (near 2°S, 150°E in Fig. 1) in September; saturation events late in the month are rare in the overall dataset but chosen here for special interest. (c) NSIPP2 model at 8°N, 140°E in July.

periodic small domain) models, indicating temperature anomalies of + 3 K and greater relative to the initial state. Observed tropical temperature fluctuations are much smaller: red dotted contours can be glimpsed only occasionally near 100 mb in Fig. 3a, never in the troposphere. These ''hot'' anomalies occur in association with very low RH and are caused by advective tendencies due to imposed subsidence. Once present, these hot dry layers sit atop a base of stable stratification, resisting convection and thus staying dry. There is no physical process capable of opposing this adiabatic warming except longwave cooling enhancement by the Planck function, which is weak and counteracted by reduced emissivity in dry conditions. Conceivably this strong imposed upper-level subsidence (corresponding to strong diagnosed cooling in Fig. 3b) was real, perhaps driven by evaporative cooling from condensed water that in nature was horizontally advected into the array. However, the low RH in association with the cooling (e.g., around days 214 and 220) make the presence of large amounts of condensate seem unlikely. Perhaps these are simply errors in observed wind divergence that were not corrected by gross adjustments for column-integrated mass or energy conservation. Correspondingly large cold anomalies are never seen, even in the global models, since excesses in forced adiabatic cooling aloft efficiently provoke convective heating responses.

Figure 4a shows CAM3 output from a similarly rainy marine location (the IFA, I on Fig. 1, in January). Compared to observations, CAM3 rain events appear blocky rather than spiky, with long flat stretches at $R \sim 0.5$–1 mm $h^{-1}$ (giving a peak in the distribution function; DeMott et al. 2007). Rain events repeat about every three days. Deep RH variations are not seen with CAM3 rain events: instead, high RH values are seen at three levels in the troposphere, varying apparently independently, except that upper anomalies descend to midlevels sometimes. Condensed water has some intense maxima (voids inside blue contours) in association with saturated (black) RH values at midlevels. Upper clouds have little condensed water, usually exceeding only the special smallest value contour (2 mg $kg^{-1}$).

Cloud fraction in CAM has two parts: a convective part that accounts for the vertical black contours in Fig. 3a that parallel the red pillars of Q1, and a part diagnostically related to RH, which generates the more horizontally oriented features paralleling RH, including the large cloud fraction at upper levels and the secondary layer of frequent cloudiness at midlevels. Convective cloud fraction frequently occurs in the absence of any condensed water, and so has no radiative impact (e.g., near days 29−30, below the uppermost troposphere). As in the forced rain events of Fig. 3c, ''toe'' structures of low-level cloudiness are often seen immediately preceding rain events after dry intervals (e.g., on days 3, 6, 8, 16, 23, and 26).

Data from the AM2, for a wet month over Manus at 2°S in the equatorial western Pacific, are shown in Fig. 4b. The intense events late in the month are actually quite rare; most of the site months are more like the first half of the month here. Rain is continuous, and exhibits multiday variations that are fairly coherent with RH over a deep layer in the lower troposphere, presumably reflecting the highly moisture-sensitive entraining plumes of the model's version of the relaxed Arakawa–Schubert (RAS) convection (Moorthi and Suarez 1992). The time sequence is also punctuated by occasional sharp transitions and spikes in rain rate and upper-level RH, indicative of a switching behavior in the convection. Condensed water is widespread in the section, often in discrete lobes in the vertical, corresponding to preferred detrainment altitudes that the convection scheme settles into and sustains through the shape of its effects on the stability profile (evident in single-column experimentation; not detailed here). Cloud fraction (solid contours) is largest in the upper troposphere and is prognostic, so it is not trivially related to rainfall or condensed water. In the lower troposphere, cloud fraction rarely exceeds 15% (two contours) in the more representative first half of the month, with a pattern that often corresponds to the condensed water lobes and layers noted above.

Late in the month, rare events of very large condensed water are seen, in association with RH values of 100% and hot $T$ anomalies (3 K) in the troposphere—remarkable for a grid point within 5° of the equator (a strong midlevel horizontal circulation was present; not shown). Such grid-scale saturation events, while relatively rare, play a significant role in this model's radiative climate through indirect mechanisms that are correlated, but not necessarily collocated, with the occurrence of large-scale surface rain (Held et al. 2007). Figure 4b suggests that their direct effects may also be significant, as TOA radiation outputs for this case (not shown) indicate a strongly negative net cloud forcing whenever these saturated layers are present, even though they create essentially no large-scale rain at the ground in Fig. 4b (dotted green line exceeds 0 only slightly, once, during day 263). Although little rain reaches the surface, an intense evaporative cooling of several kelvin per day (blue) is seen beneath the upper-level saturated region on day 268.

A third contrasting style of convective events is seen in Fig. 4c, for 35 days around July in the NASA model over a rainy tropical ITCZ location at 8°N, 140°E. The

rain-rate time series has rich variations in terms of both time scale and values, with few plateaus during irregular ~1 day long events with shaggy faster variations. Rain rate rarely shrinks truly to zero. Much of the total rain (solid green curve) falls from the large-scale cloud schemes (dotted green curve), including the anvil scheme (red dotted curve). This is especially true during four major upper-tropospheric saturation events (black regions in RH plot) near days 4, 11, 16, and 26–29. Beneath these upper saturation regions, cloud water is reduced to low values, presumably by rain scavenging and evaporation (negative Q1 values in the lower troposphere). Cloud fraction is 100% in these events (voids inside black contours). Between these events, rain is predominantly or totally convective, often in middle-depth convection (e.g., in the last 3 days of section), with positive Q1 confined mainly to the lower troposphere. These moderately deep convective events detrain decaying pulses of condensate and associated pulses of cloud fraction in the middle to upper troposphere, causing intense localized radiative heating/cooling rate spikes (small red and blue patches, often hidden by cloud fraction contours).

In summary, impressions above indicate a very different character to deep convective events among the three GCMs, and between these and observations. To reduce the dimensionality and subjectivity of these comparisons, it is useful to construct characteristic or composite events.

## 5. Regression diagrams

### *a. From 1 month of observations*

A standard technique for extracting characteristic structures from complex data is lagged linear regression of time series of predictands against a predictor time series. Since the predictands are functions of height, the resulting diagrams are lag–height sections. Many examples using observations at various scales may be viewed in Mapes et al. (2006); the same codes were used for this paper. Other methods of composite event construction were tried and give qualitatively similar results.

Regression sections versus total surface rain rate were made for every site month, for lags extending from −3 to 3 days. Single-month results are illustrated in Fig. 5, obtained from the same KWAJEX data shown in Fig. 3. Regressions of upwelling top-of-atmosphere radiation (Fig. 5a) are presented in a time integrated (cumulative) manner, normalized by the positive area under the rain autocorrelation curve, with units of kilojoule of anomalous TOA outgoing radiation per millimeter of accumulated surface rainfall. Curves are shown from both satellite observations included with the cloud model forcing data (LW = dotted, negative; SW = dashed, positive; solid = net) and cloud model outputs (all three terms dash–dotted; the order of curves follows the satellite observations). The cold-topped, visually white nature of cloudiness in deep convective weather guarantees a cancellation of LW and SW effects. In both datasets the main radiative impacts occur within a day around lag 0, although the model's net radiation curve incurs a negative increment before lag −2, which seems unlikely to be a statistically robust result. The cloud model's rain-associated clouds appear to be insufficiently reflective around day 0, perhaps related to low-biased mean albedo noted in the simulation by Blossey et al. (2007).

Regression sections of condensed water and cloud fraction (from the cloud model) and RH (from observations; the model field is similar) are plotted in Figs. 5b,c,e, with the autocorrelation of rain rate indicated beneath each lag-pressure section. Both RH and cloud water exhibit deep vertically coherent positive anomalies around lag 0. Lower-tropospheric RH anomalies are greatest a few hours before rainfall, while midlevel humidity peaks after rain and lingers for ~2 days in a thinning layer around 500 mb. Cloud water and fraction have a somewhat similar tilt toward positive lags with height, but are centered more narrowly on rain-rate anomalies (rain rate from the model was used for these plots, to avoid the ~2 h lag between budget-diagnosed rain rate and model rain rate when forced by those same budget terms).

Horizontal wind divergence (Fig. 5e) is indicative of the mesoscale (hundreds of kilometers) mean vertical motions associated with rain events. Interpreting positive values as convective outflow, cloud tops apparently rise from about 800 to 500 to 200 hPa, leading up to peak rainfall, as seen for other field campaign datasets in Mapes et al. (2006). Convergence ascends from low to middle levels across lag 0, a characteristic feature of the mesoscale convective system (MCS) life cycle, while surface divergence persists for a day after rain, associated with mesoscale as well as convective downdrafts (Zipser 1977). In multiscale observations, this surface signature fades with spatial averaging, as convergence at the edges of the outflow cancels the divergence in the middle (Mapes et al. 2006, 2009; Folkins et al. 2008), so its absence in the models (shown below) may not necessarily be as incorrect as it appears.

The temperature pattern (Fig. 5f) is also consistent with prior results but is hard to interpret directly in terms of physical processes, except for the cool surface air after rain. This cold surface layer and the rest of the tripole vertical structure around lag 0 are robust and familiar (e.g., Sherwood and Wahrlich 1999).

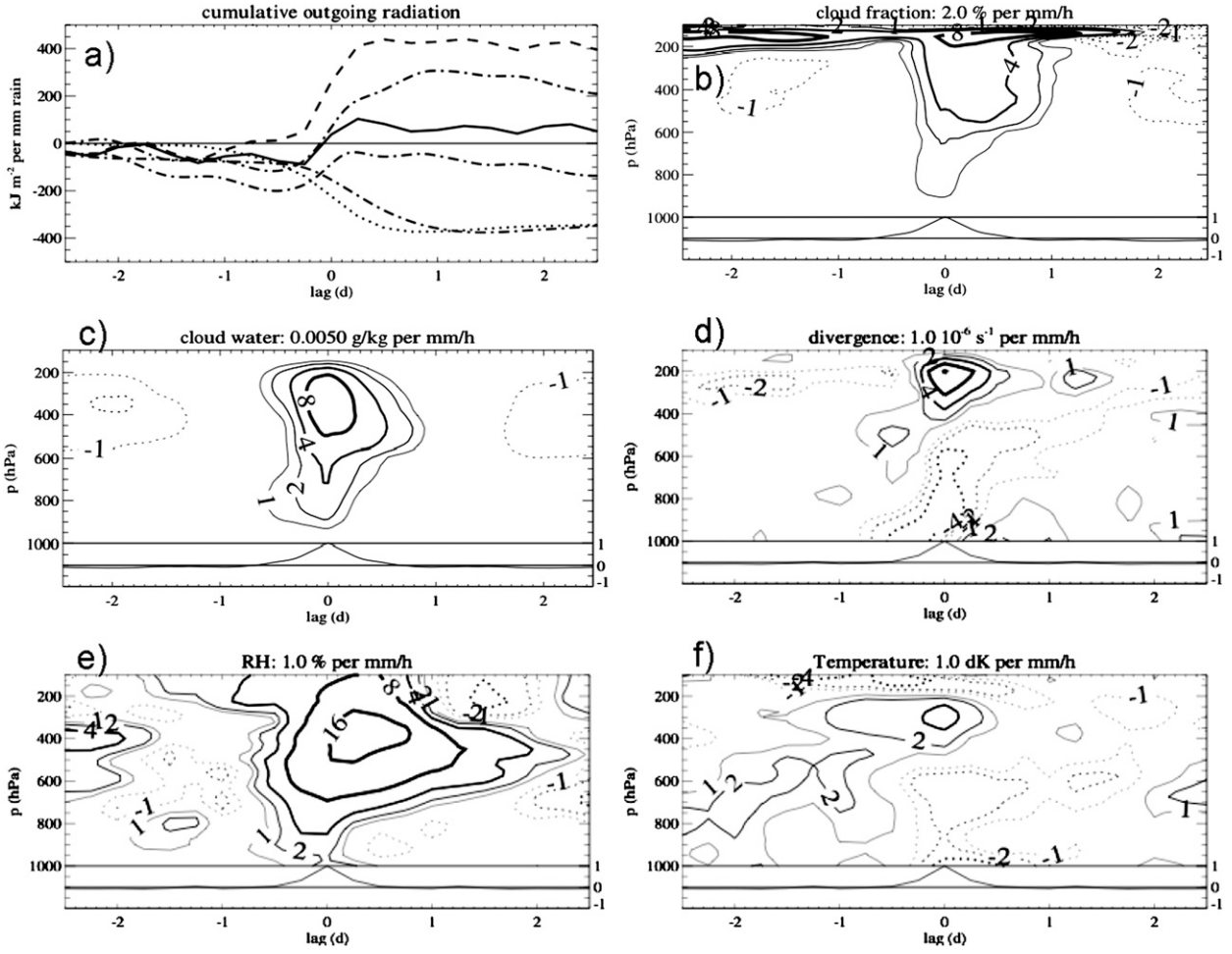


FIG. 5. Lagged regression composites of KWAJEX submonthly variations of the indicated fields. The base time series is surface rain rate. (a) Regressions of upwelling radiation, in cumulative form (obs: dotted, dashed, and solid; model: all dashed–dotted; see text for further explanation), and (b)–(f) regressions as indicated, using RH and divergence from KWAJEX observations and clouds from the cloud model.

### *b. Composites of regression sections from multiple site months*

For clarity and robustness of results, it is desirable to combine the many available submonthly regression structure results, like Fig. 5, into a single diagram characterizing GCM tropical rain events. Site months with little or no rain yield noisy or undefined regressions, and so must be excluded. Some extratropical weather events are surely included (in light of column locations, Fig. 1), but these do not change the results enough to fuss with defining, detecting, and excluding them. On the basis of Fig. 2c, we combine the regression sections of all rainy marine site months for each model, using simple averaging and significance testing as discussed in section 2, to produce Figs. 6–8. These are directly comparable to Fig. 5, and for brevity we will call them characteristic rain event structure plots.

The CAM3 characteristic rain event structure, from 33 site months, is shown in Fig. 6. In Fig. 6a an ensemble of 10 Monte Carlo subset composites brackets sampling uncertainties in the cumulative radiation presentation. Longwave trapping effects extend through lag + 2 days, to finally exceed shortwave reflection effects in this space of linear regression coefficients (quantitative interpretations should probably not be taken too far).

In the other panels, shading indicates statistical significance of the sign of each field within the additive composite. At negative lags, significant RH and divergence anomalies appear to indicate shallow convection building up for about 2 days prior to rain. Scrutiny of the rain autocorrelation suggests a mild 3-day periodicity; note also the 10 rain events in 30 days in Fig. 4a. The strongest signals are near lag 0 (note logarithmic contour interval). Just before rain, RH immediately above

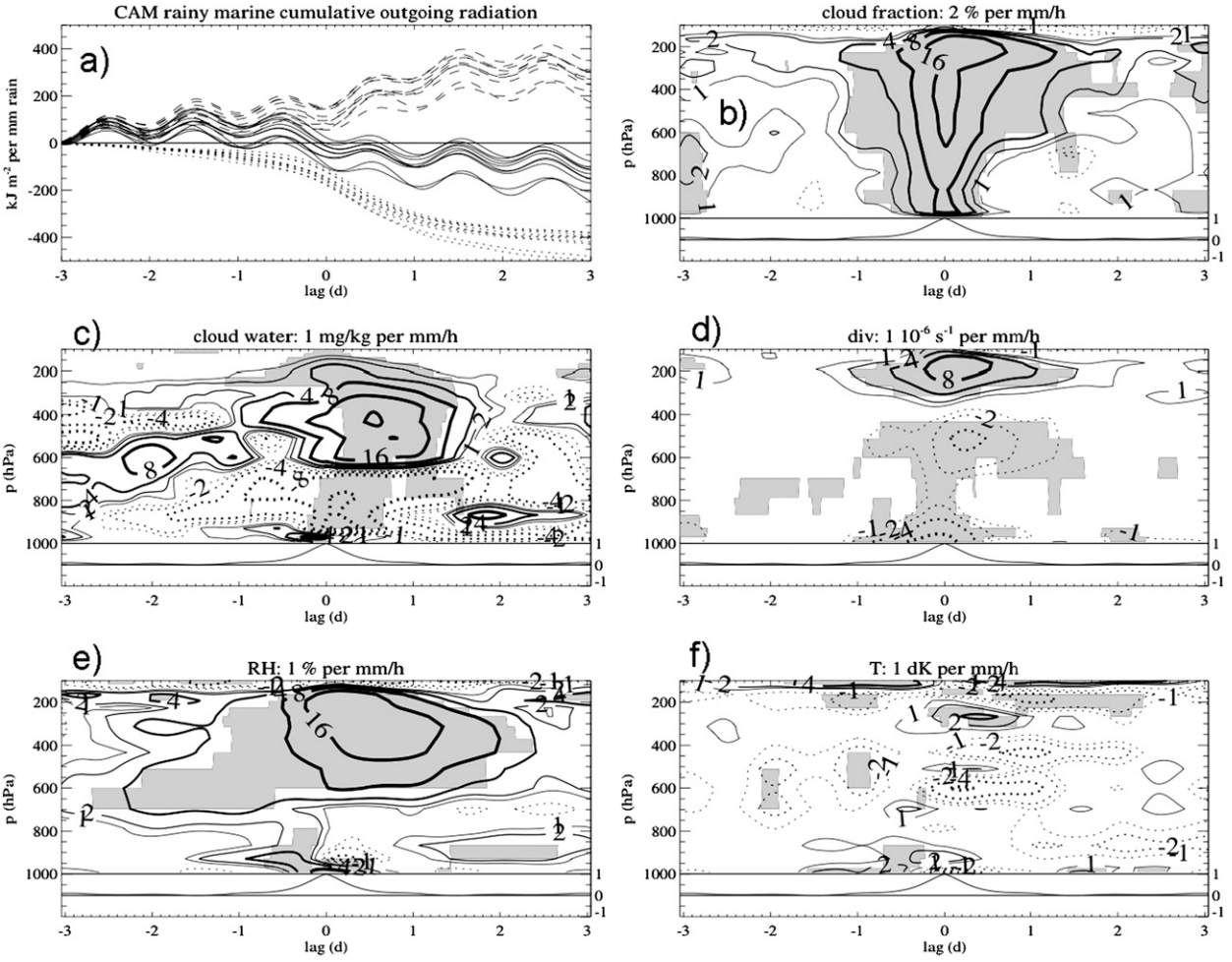


FIG. 6. Simple additive composites of lag-regression diagrams like Fig. 5 for 33 rainy marine months in CAM3. Shading indicates statistical significance of the lag–height fields (where the composite mean exceeds the standard deviation divided by $33^{1/2}$), while in (a) the ensemble of curves shows composite means for 10 randomized subsamples of the 33 months, with the expectation value of subsample size equal to half the full sample (16.5 in this case).

the boundary layer accumulates and then jumps down to the surface where it can trigger the penetrative deep convection scheme. A vertical column of total cloud fraction (convective plus large scale) shows the event, while cloud water becomes large only in midlevels, with negative anomalies seen in the lower troposphere. It is notable that quite large midlevel cloud water fluctuations at lags larger than a day remain statistically insignificant: this indicates strong cloud variations that are incoherent with rain, as seen in Fig. 4a. CAM3 upper-level divergence spans about a 2-day period, with convergence ascending from low to middle levels during the rain. However, no surface divergence is seen at positive lags, and cold surface air there is feeble and not statistically significant, suggesting that downdraft processes are too weak. Upper-level RH and cloud water descend through the upper troposphere after lag 0, as seen in Fig. 4a. These CAM3 results are in agreement with the findings of DeMott et al. (2007), and extend them. Further subdivisions of the months seem impractical, as statistical significance is already limited in coverage (gray) with the 33 months here.

The AM2 rain events have a very different character (Fig. 7), most obviously a long time scale (almost a week). SW and LW CRF are nearly balanced, from a cloud population that is distinctly bimodal in the vertical, as seen in both cloud fraction and condensed water. These layers probably reflect the convection scheme's separate treatment of plumes detraining below 500 hPa (with no cloud work function threshold) and those detraining above (often the least dilute, subject to a tuned set of top-dependent thresholds that are set to permit tropopause depth convection). Divergence also shows two distinct layers of outflow, while convergence is

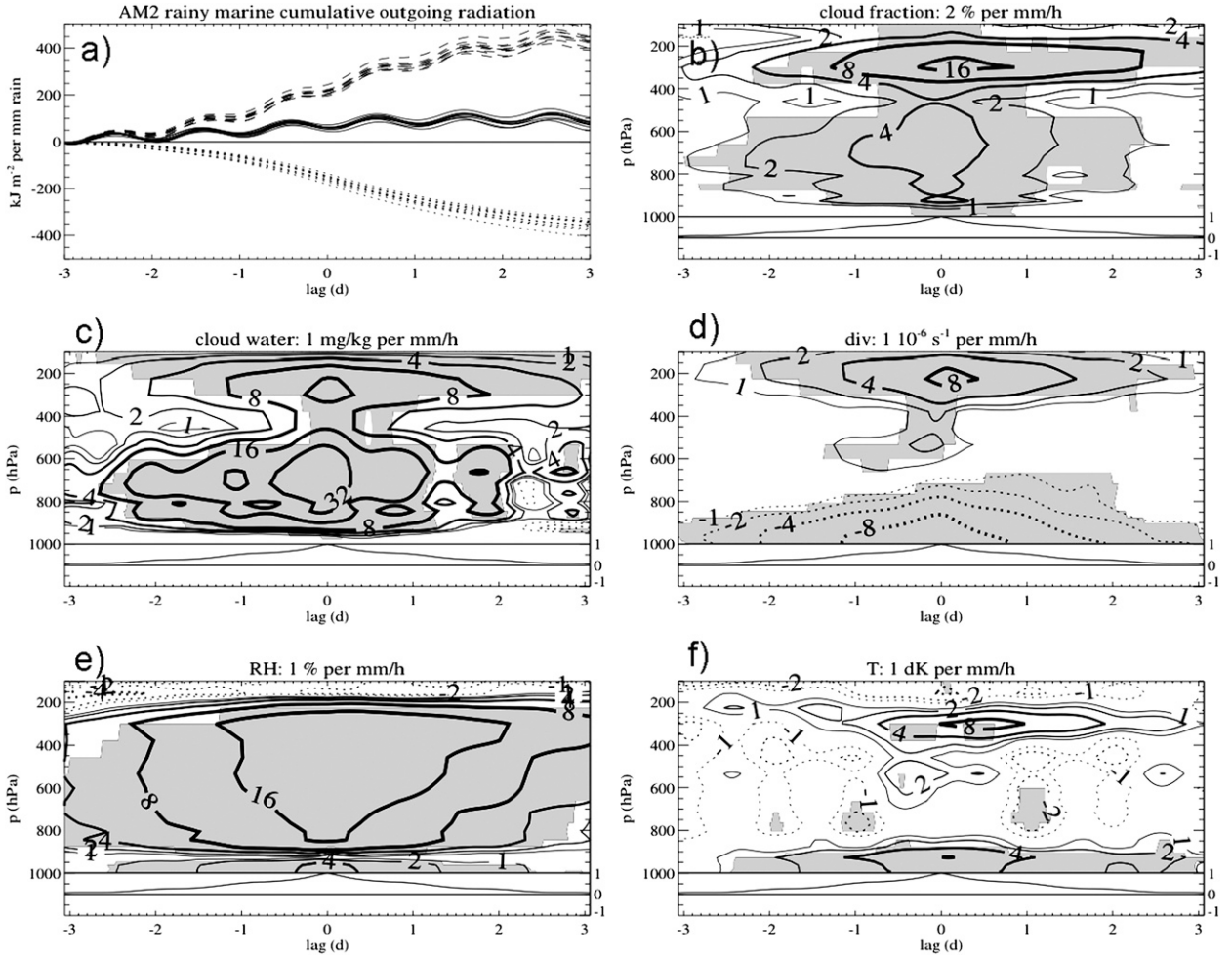


FIG. 7. As in Fig. 6 but for 47 rainy marine months in AM2.

confined to low levels and persists throughout all lags. Surface air is anomalously warm and moist in rain events, although RH exhibits a distinctive node at about 925 hPa.

NSIPP2 model characteristics (Fig. 8) include a predominance of shortwave reflection over longwave trapping, consistent with the large negative monthly mean CRF in the highly rainy columns analyzed here (''N'' symbols in Fig. 2a). The jellyfish-like upper-troposphere cloud water anomalies, with reduced cloud water below as seen in Fig. 4c, appear clearly in the regression, even though cloud fraction (and the very similar RH field) are positive through the troposphere in connection with rain events. Shallow convection developing upward in advance of rain is indicated by the tilt of RH, cloud, and divergence contours. Convergence ascends into the middle troposphere during rain but, again, surface divergence does not develop after rain. A thin layer of significant cool surface air does appear around lag 0, driven by convective downdrafts.

Rainy land results from AM2 and CAM3 are not shown here, but deserve mention. At first glance, they appear very different: they have strong diurnal oscillations, whose phase structure is certainly of interest but beyond the scope of this paper. However, a 24-h smoothing reveals results remarkably similar to similarly smoothed versions of the rainy marine composites above (not shown). Evidently the character of the processes governing ''free'' convection (as seen over the oceans) in each model is fairly robust to the addition of a strong fast forced (diurnal) oscillation.

## 6. Summary and discussion

Time–height GCM outputs of tropical cloud fields and processes have been examined, from three global models as well as KWAJEX observations and an observation-forced cloud model, including cloud radiative forcing aspects. The observations examined here are similar to those from other field campaign data

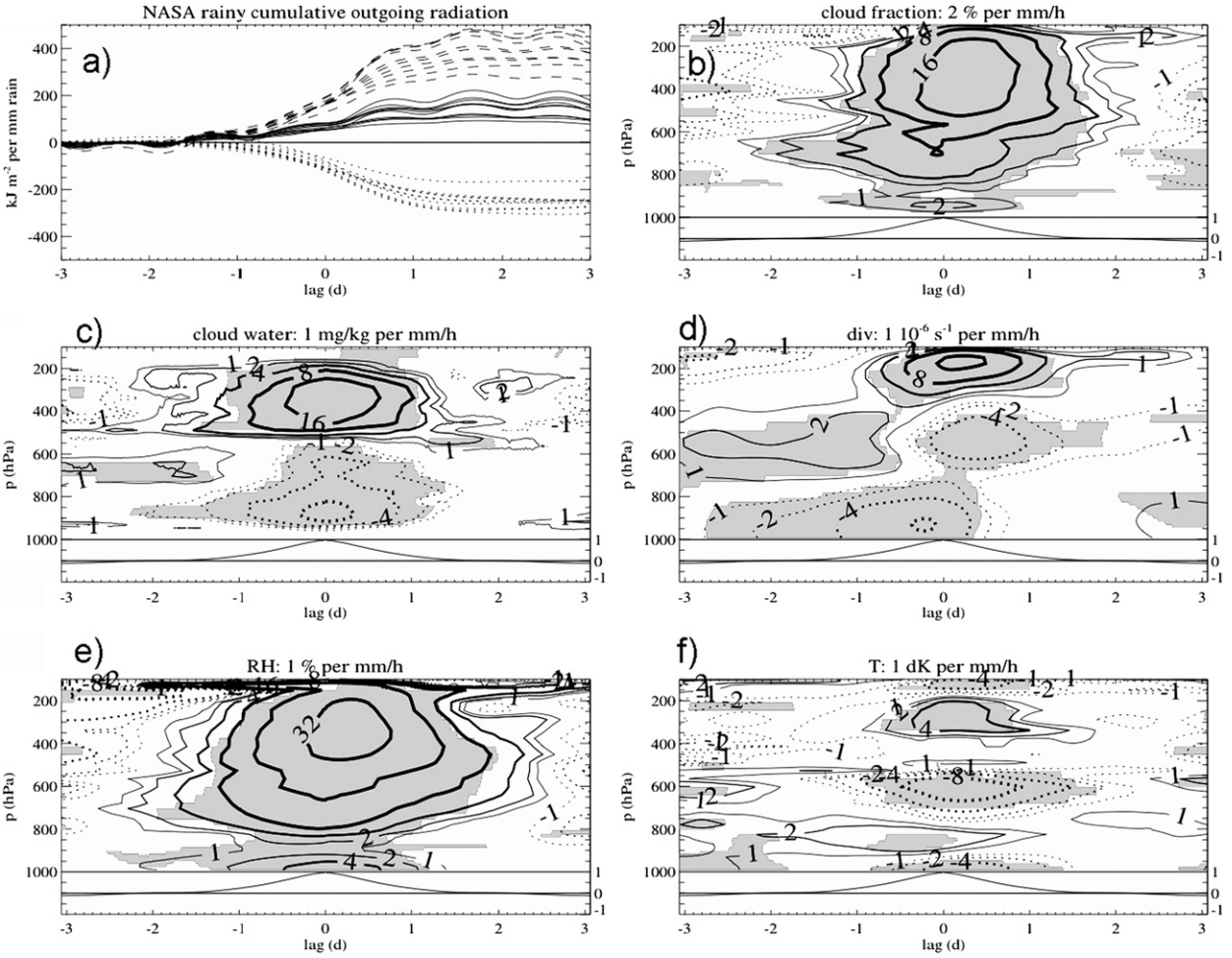


FIG. 8. As in Fig. 6 but for 8 rainy marine months from the NSIPP2 model.

(DeMott et al. 2007; Mapes et al. 2006). Forced cloud model outputs appear to be reasonably accurate, except for understandable artifacts of the forcing protocol: for example, no physical cooling process exists to counter excessive subsidence warming that may be prescribed from erroneously diagnosed downward motions in nature.

Deep convective processes in the models are very different—from observations and from each other. Many aspects of the characteristic structures of convective weather events in the models can be understood in light of model physics. The weakness of downdrafts in association with rain appears to be a common model error, one which might be linked to important consequences at larger scales (Bacmeister et al. 2006). On the other hand, observations of post-rain divergence are scale dependent (Mapes et al. 2006; Folkins et al. 2008), so perhaps models can be charitably viewed as accurate but at a coarse effective horizontal resolution.

The occurrence of large-scale saturation appears to signal a qualitatively different type of cloudy weather in the GCMs. This saturation occurs in tandem with parameterized convection, a situation which may be viewed as a gentle, formally scale-separated version of the real case of Mesoscale Absolutely Unstable Layers (MAULs) (Bryan and Fritsch 2000). Equating this grid saturation process (or large-scale cloud scheme rainfall) with the observed phenomenon of stratiform precipitation in nature (Houze 1997), as implied in some model evaluation discussions, seems too simplistic. Still, there does seem to be a real qualitative distinction at issue.

How should models manage such saturation events? The answer is unclear, not only from a purely physical realism perspective but also in light of numerical inaccuracies near the grid scale. Preventing then is not necessarily desirable: for example, the NASA model's MCS-like convection events, in which multiple schemes all interact with grid saturation, appear quite realistic in

many senses. One memorable image, from mesoscale modeler J. Kain (2005, personal communication), is that a convection scheme can be thought of as analogous to the control rods in a nuclear reactor, permitting but managing the powerful ''chain reaction'' of explicit saturated overturning. In the GCMs examined here, saturation events have a strong net TOA cloud radiative forcing (cooling the planet). Their substantial influence (both direct and indirect) on the subtle question of cloud feedbacks on climate change (Held et al. 2007) is distressing, in light of their gridpoint scale (as seen in neighboring column analyses, not shown) and the dependence of occurrence statistics on model mesh spacing.

Comparing model weather to observations via this ''virtual field campaign'' approach seems a useful addition to the suite of available model evaluation methods. Field observations clearly should have a role to play in climate model improvement and credibility evaluation, but bringing them to bear is not straightforward. Forcing a model to track observed weather explicitly is another fruitful tactic (Boyle et al. 2008), although model offset biases (discoverable by simpler means) intrude via spinup shocks, so the more literal (time aligned) observation–model comparisons gained may reflect imperfectly on how schemes will really interact in free runs.

The sample size used here (tens to hundreds of site months) seems adequate, especially if observational databases of similar sample size are the basis for comparison. Unfortunately, observational campaigns have often been conducted near land or on otherwise complex geographical settings that make comparisons to nominally collocated coarse model column data challenging to interpret. In addition, letting observational field campaign availability guide the sampling of models risks leaving important regimes and rare events (like tropical cyclones, in nature and gridpoint storms in models) un- or undersampled.

While larger datasets of high time and height resolution GCM data could easily be created, the more-is-better theory of output raises real questions about data access and analysis strategy in the face of finite effort levels. Hierarchical or telescoping datasets seem most useful: Coarse summary statistics (e.g., Fig. 2) can provide useful index information for planning the mining of the larger detailed database (like the objective regime definitions used here), and for interpreting the results of finite samples.

High-resolution reference simulations are becoming another important, but dauntingly voluminous, source of pseudo-observational data that in principle should be useful for improving climate models. There too, it seems promising to generate datasets resembling those from field campaigns. The KWAJEX-driven cloud–model data used here (Blossey et al. 2007) are a good example of such a strategy. In this case, the time–height dataset created by M. Khairoutdinov characterized the whole model domain ($256 \times 265$), but as larger (regional and even global) explicit convection simulations are performed, similar datasets could be created for selected subsets of the domain. This subsampling would be akin to field campaigns with radar and/or sounding arrays, but with perfect precision in all fields. With such datasets, process-scale structures could be examined, within well-characterized large-scale contexts, using familiar tools that link the activity to observations.

Coordination seems critical to the success of virtual field campaign strategies. For maximum utility, output generation codes should be designed by the likely analysts of the resulting datasets. These may need to be implemented deep inside models at run time, especially for big computations where entire domain outputs are impractical to create and/or hard to postprocess. At the same time, diagnostic efforts are only effective toward model improvement when results are readily available in a tight interaction loop with model development trials. Offline diagnostics as described here, however informative, can only have limited and long-delayed impact unless they are automated and made available during experimentation. This was precisely the vision of the Climate Process Team project, which spawned this paper, so in a sense our work is simply incomplete.

Of course, it remains an unproven conjecture that designing and tuning physical processes to simulate the texture of cloudy weather events will reliably improve global mean and longer-term aspects of climate model performance. Still, aiming for qualitative correctness in simulations of well-observed phenomena seems like a virtue in its own right, and full NWP-type evaluations of climate models remain difficult. In the end, there may simply be no other way to increase confidence in long integrations of climate models than by aiming to make them simulate fast physical processes well within realistic depictions of weather.

*Acknowledgments.* This material is based upon work supported by the National Science Foundation under Grant ATM0555796. Ming Zhao was supported under Award NA17RJ2612 from the National Oceanic and Atmospheric Administration, U.S. Department of Commerce. We thank PI Chris Bretherton and the entire Climate Process Team on low-latitude clouds for vital inputs and feedback, and three reviewers for many manuscript improvement ideas. Correspondence with Peter Blossey, Charlotte DeMott, and Matt Wyant also improved the paper.

## REFERENCES


Bacmeister, J. T., M. J. Suarez, and F. R. Robinson, 2006: Rain reevaporation, boundary layer convection interactions, and Pacific rainfall patterns in an AGCM. *J. Atmos. Sci.,* **63,** 3383–3403.

Blossey, P. N., C. S. Bretherton, J. Cetrone, and M. Khairoutdinov, 2007: Cloud resolving model simulations of KWAJEX: Model sensitivities and comparisons with satellite and radar observations. *J. Atmos. Sci.,* **64,** 1488–1508.

Bosilovich, M. G., and R. Lawford, 2002: Coordinated Enhanced Observing Period (CEOP) international workshop. *Bull. Amer. Meteor. Soc.,* **83,** 1495–1499.

Boyle, J., S. Klein, G. Zhang, S. Xie, and X. Wei, 2008: Climate model forecast experiments for TOGA COARE. *Mon. Wea. Rev.,* **136,** 808–832.

Bretherton, C. S., 2007: Challenges in numerical modeling of tropical circulations. *The Global Circulation of the Atmosphere,* T. Schneider and A. H. Sobel, Eds., Princeton University Press, 302–330.

Bryan, G. H., and M. J. Fritsch, 2000: Moist absolute instability: The sixth static stability state. *Bull. Amer. Meteor. Soc.,* **81,** 1207–1230.

DeMott, C. A., D. A. Randall, and M. Khairoutdinov, 2007: Convective precipitation variability as a tool for general circulation model analysis. *J. Climate,* **20,** 91–112.

Folkins, I., S. Fueglistaler, G. Lesins, and T. Mitovski, 2008: A low-level circulation in the tropics. *J. Atmos. Sci.,* **65,** 1019–1034.

Held, I., M. Zhao, and B. Wyman, 2007: Dynamic radiative–convective equilibria using GCM column physics. *J. Atmos. Sci.,* **64,** 228–238.

Houze, R. A., 1997: Stratiform precipitation in regions of convection: A meteorological paradox? *Bull. Amer. Meteor. Soc.,* **78,** 2179–2196.

Johnson, R. H., and P. E. Ciesielski, 2000: Rainfall and radiative heating rates from TOGA COARE atmospheric budgets. *J. Atmos. Sci.,* **57,** 1497–1514.

Lin, J. L., and Coauthors, 2006: Tropical intraseasonal variability in 14 IPCC AR4 climate models. Part I: Convective signals. *J. Climate,* **19,** 2665–2690.

Mapes, B. E., S. Tulich, J. L. Lin, and P. Zuidema, 2006: The mesoscale convection life cycle: Building block or prototype for large scale tropical waves? *Dyn. Atmos. Oceans,* **42,** 3–29.

——, R. Milliff, and J. Morzel, 2009: Composite life cycle of maritime tropical mesoscale convective systems in scatterometer and microwave satellite observations. *J. Atmos. Sci.,* **66,** 199–208.

Moorthi, S., and M. J. Suarez, 1992: Relaxed Arakawa–Schubert: A parameterization of moist convection for general circulation models. *Mon. Wea. Rev.,* **120,** 978–1002.

Randall, D. A., K. M. Xu, R. J. C. Somerville, and S. Iacobellis, 1996: Single column models and cloud ensemble models as links between observations and climate models. *J. Climate,* **9,** 1683–1697.

Sherwood, S. C., and R. Wahrlich, 1999: Observed evolution of tropical deep convective events and their environment. *Mon. Wea. Rev.,* **127,** 1777–1795.

Silva Dias, M. A. F., and Coauthors, 2002: Cloud and rain processes in a biosphere-atmosphere interaction context in the Amazon region. *J. Geophys. Res.,* **107,** 8072, doi:10.1029/2001JD000335.

Sobel, A. H., S. E. Yuter, C. S. Bretherton, and G. N. Kiladis, 2004: Large-scale meteorology and deep convection during TRMM KWAJEX. *Mon. Wea. Rev.,* **132,** 422–444.

Wyant, M. C., C. S. Bretherton, J. T. Bacmeister, J. T. Kiehl, I. M. Held, M. Zhao, S. A. Klein, and B. A. Soden, 2006: A comparison of tropical cloud properties and responses in GCMs using midtropospheric vertical velocity. *Climate Dyn.,* **27,** 261–279.

Yanai, M., S. Esbensen, and J. H. Chu, 1973: Determination of bulk properties of tropical cloud clusters from large-scale heat and moisture budgets. *J. Atmos. Sci.,* **30,** 611–627.

Zipser, E. J., 1977: Mesoscale and convective-scale downdrafts as distinct components of squall-line structure. *Mon. Wea. Rev.,* **105,** 1568–1589.